Supramolecular adaptive nanomotors with magnetotaxis behavior

Supramolecular Adaptive Nanomotors with Magnetotaxis Behavior

*Fei Peng, Yingfeng Tu, Yongjun Men, Jan C. M. van Hest, and Daniela A. Wilson**

Synthetic nano- and micromotors have become a central research topic since the report of their first prototype, centimeter-sized motor.[1] In mimicking natural molecular motors[2] or moving micro-organisms,[3] these motors convert locally supplied chemical energy into motion, showing prospects in revolutionizing various fields such as microsurgery,[4] targeted drug delivery,[5] sensing,[6] imaging,[7] and environmental remediation.[8] However, motors in general and especially nanoscale motors, are susceptible to random fluctuations,[9] therefore navigation of autonomous motors remains challenging. Compared to natural motors, synthetic motors are insufficient to perform complex functions. To tackle this challenge, recent efforts have been dedicated to develop motors able to respond to environmental clues such as temperature,[10] external field,[11] and light.[12] Only a few recent reports[13] have shown that motors can navigate themselves according to local stimuli and the stimulatory gradients. Among these, magnetic-field gradients and magnetic fields provide a wireless, non-invasive way to gain control over the motion of these motors. In nature, magnetotactic bacteria (*Magnetospirillum magnetotacticum*), which possess iron oxide crystals in their body,[14] can sense the external magnetic field and reorient themselves to the direction of Earth's magnetic field. Inspired by this, we set out to explore the possibility of gaining directional control by integrating magnetic segments into our supramolecular motors[5c] (**Figure 1**) and steer the motor using both gradient magnetic field as well as by changing the direction of a homogeneous magnetic field. Due to their minimal invasive nature, external magnetic fields are compatible with most living systems and widely used for drug delivery[15] and imaging.[16] When compared with optical, electrical, or acoustic fields, magnetic fields offer the highest flexibility concerning achievable forces.[17] Using magnetic fields to remotely manipulate nanomotors in a biological medium allows safe maneuvering.[18] However it remains a question whether dynamic motors could be precisely manipulated at nanometer scale and move within a micron-sized confined space such as tumor tissue-related environment.

Here, we demonstrate the design of magnetically actuated stomatocyte nanomotors, which could achieve guided autonomous motion. Going beyond the conventional top-down method to incorporate a magnetic component,[19] we adopted a bottom-up approach which is familiar to natural systems and introduced magnetic metallic nickel in situ with the catalytic platinum nanoparticles (PtNP). In this way the geometric asymmetry of the system was not compromised and the co-presence of both nickel and platinum in stomatocytes was ensured. The movement of our original supramolecular nanomotors was powered by catalytic decomposition of hydrogen peroxide, which is an interesting biologically relevant signaling compound related with tumor cell metastasis and invasion.[20] After incorporating the magnetic nickel component, the synthetic motor was able to function in dual mode (catalytically powered by PtNP or magnetically powered by magnetized nickel). Furthermore, this design also provided the possibility for simultaneous guiding and steering of catalytically powered motors with additional magnetic fields. A collagen gel matrix laden with human cervical cancer HeLa cells was used as a tumor tissue model to demonstrate the guided motion of nickel incorporated nanomotors. Being in the nanometer scale regime, the nanomotors were readily guided into the micrometer-sized gel mesh. In addition, like other self-assembled motors,[21] the supramolecular motors can be easily fabricated and easily loaded with drugs and have good biocompatibility in biomedical fields. Able to operate with multiple energy sources, nanomotors presented in the paper promise to expand the applicability of the motors and address comprehensive biomedical challenges.

Bowl-shaped polymersomes or stomatocytes were assembled from diblock polymer poly(ethylene glycol)$_{44}$-*block*-polystyrene$_{190}$ via a controlled shape transformation.[22] The poly(ethylene glycol) segment allows the vesicles to be biologically stealthy and reduces the possibilities of immune attack and clearance. By adding preformed dendritic platinum nanoparticles into the polymer organic solution during self-assembly, nanoparticles were entrapped into the outer cavity of the stomatocytes (Figure 1). The loaded platinum nanoparticles serve as catalyst to decompose hydrogen peroxide into oxygen and are responsible for the propulsion of the entire system. The fluorescent anticancer drug doxorubicin (Dox), as a model drug, was mixed with the organic solvent containing the polymer, and was enclosed in the original lumen of the stomatocyte. After self-assembly and shape transformation into doxorubicin- and PtNP-loaded stomatocytes, metallic nickel was grown in situ directly onto the platinum nanoparticles, serving both as catalyst and substrate.[23] Figure 1 summarizes the experimental procedure for preparing the platinum–nickel-loaded stomatocytes. In the presence of reducing agent hydrazine, a nickel-ion–hydrazine complex was first formed, followed by the reduction to metallic nickel by the platinum catalyst. No additives or stabilizers were needed. The reduction reaction was allowed to run at 40 °C for 2 h. After 2 h, the reaction was stopped. Ultrafiltration was used to remove unreacted hydrazine and nickel ion

F. Peng, Y. Tu, Dr. Y. Men, Prof. J. C. M. van Hest, Dr. D. A. Wilson
Institute for Molecules and Materials
Radboud University
Heyendaalseweg 135
6525 AJ, Nijmegen, The Netherlands
E-mail: d.wilson@science.ru.nl

DOI: 10.1002/adma.201604996

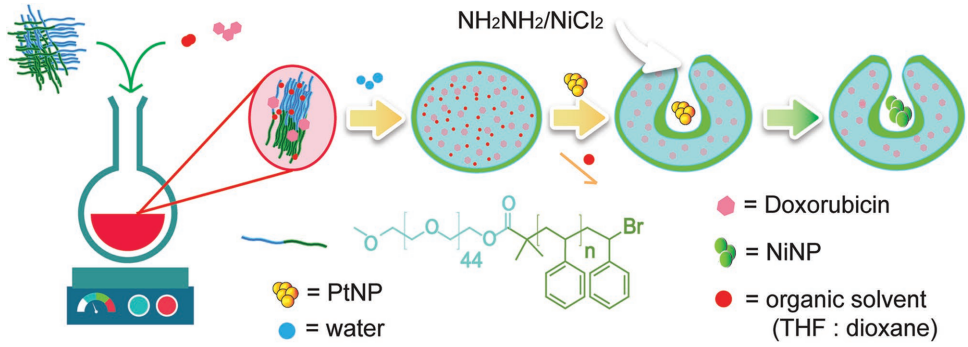

Figure 1. Preparation scheme of doxorubicin-incorporated, platinum–nickel-loaded stomatocytes.

before the energy-dispersive X-ray spectroscopy (EDX) analysis. EDX was used to show the element distribution of the structure (platinum, yellow color and nickel, green color) (**Figure 2**a–c). ImageJ 3D surface plot plugin was used to analyze EDX mapping data, allowing the imaging of the elements distribution in all directions. At a rotation angle of 0°, it was shown that nickel (green color) covered the surface of this side (Figure 2d) and increased the surface thickness. When changing the rotation angle to 120°, it could still be observed that nickel (green) deposited on surface (Figure S1a, Supporting Information, indicated by the red arrow), while in certain area platinum (yellow) was still present on surface (Figure S1a, Supporting Information, indicated by the blue arrow). Inductively coupled plasma emission–mass spectrometry (ICP-MS) further confirmed the

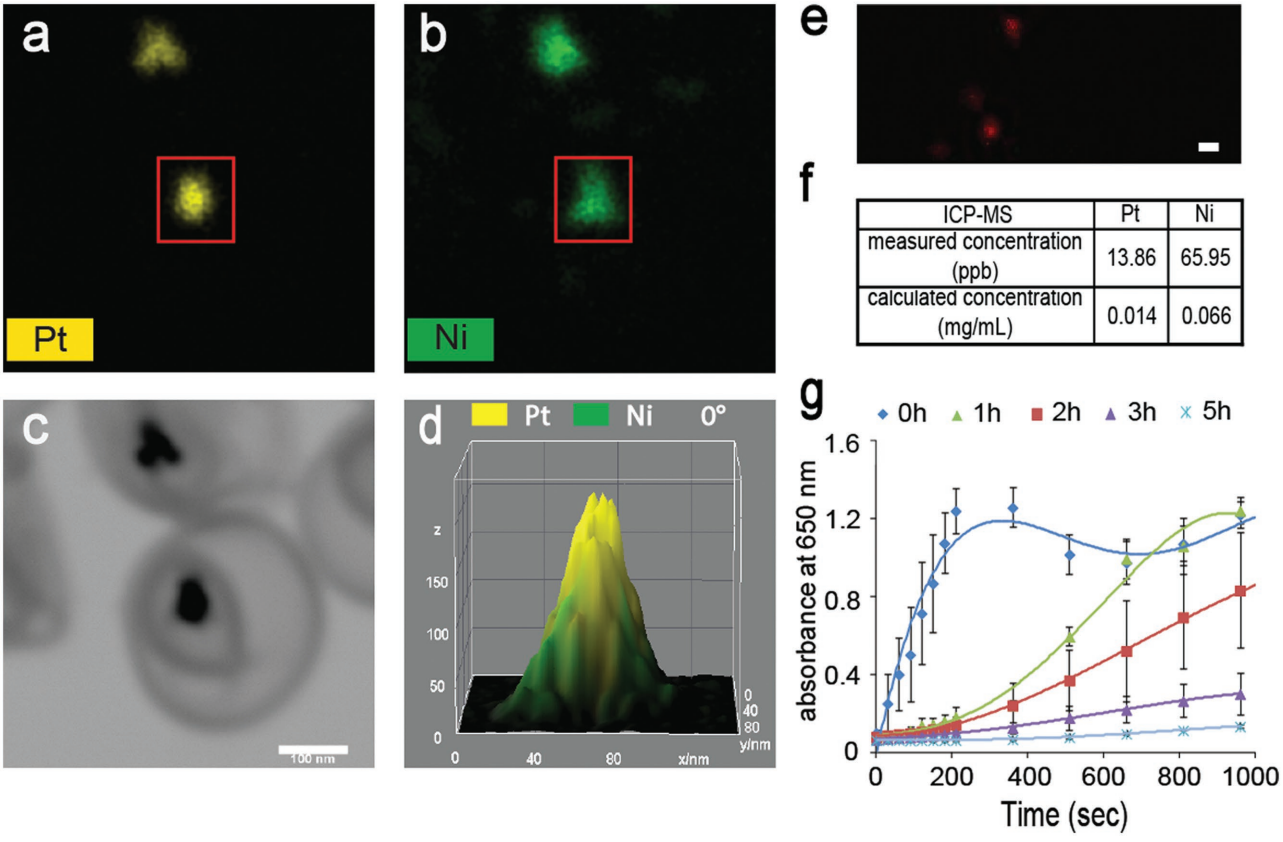

Figure 2. a–b) EDX mapping of platinum, yellow (a); nickel, green (b). c) Corresponding scanning transmission electron microscopy (STEM) image of the assembled nanomotors, scale bar is 100 nm. d) 3D surface plot profile over the cross section of a doxorubicin/platinum–nickel-loaded stomatocyte, indicated by the red square in (a) and (b), giving intensity (*z* axis) with distance over the cross section (*x*, *y* axis). e) Confocal fluorescence microscopy image of doxorubicin/platinum–nickel-loaded stomatocytes; the scale bar represents 1 µm. f) Concentration of platinum and nickel by ICP-MS. g) Comparison of reaction rate of platinum-catalyzed tetramethylbenzidine–H_2O_2 reaction for doxorubicin/platinum-loaded stomatocytes (before nickel growth or nickel-growth time 0 h, blue) and doxorubicin/platinum–nickel-loaded stomatocytes with different nickel-growth times of 1 h (green), 2 h (red), 3 h (purple), and 5 h (cyan).

presence of nickel (Figure 2f). High-magnification transmission electron microscopy (TEM) in the selected area of one platinum–nickel-loaded stomatocyte showed the diffraction pattern typical of crystalline metallic nickel (selected area electron diffraction (SAED)), demonstrating again the presence of nickel (Figure S2, Supporting Information). As mild conditions were used for the reaction, the in situ growth of nickel did not induce a change of the stomatocyte morphology or encapsulation efficiency, as was observed from representative TEM images of stomatocytes loaded only with platinum and platinum–nickel-loaded stomatocytes (Figure S3, Supporting Information). For platinum-loaded stomatocytes, the positioning of the platinum nanoparticles in the cavity of stomatocytes has been demonstrated with TEM tomography in a previous report by our group.[24] In the case of doxorubicin/platinum–nickel-loaded stomatocytes, TEM at different rotation angles along the *x*-axis was performed, showing as expected the entrapment of the particles inside the cavity of the stomatocytes (Figure S4, Supporting Information). The fluorescence signal present inside the stomatocytes demonstrated the successful loading of the fluorescent antitumor model drug Dox (Figure 2e). The fluorescence of Dox facilitates the tracking of motion with confocal fluorescence microscopy.

After growing nickel in situ, the catalytic activity of the platinum was examined to assess whether the hydrogen peroxide decomposing capability was maintained. Adding a solution of platinum–nickel-loaded stomatocytes to concentrated hydrogen peroxide (0.5% v/v) led to bubble formation, indicating the preserved catalytic activity. To quantitatively determine the catalytic activity, 3,3′,5,5′-tetramethylbenzidine–H_2O_2 assay was used.[25] 3,3′,5,5′-Tetramethylbenzidine was oxidized by hydrogen peroxide in the presence of platinum nanoparticles to blue 3,3′,5,5′-tetramethylbenzidine diimine and the reaction speed was quantitatively related with the catalytic activity of platinum. As demonstrated in Figure 2g, catalytic activities experienced a decrease after nickel growth for 2 h, yet a clear residual activity was still present. We speculate that the preservation of Pt catalytic activity is caused by a partial surface covering of the platinum nanoparticles by the nickel layer and the high branching and porosity of the dendritic platinum nanoparticles. It was speculated that the catalytic activity can be therefore preserved as long as the grown nickel does not form a complete shell over the particle, which can block all the catalytic branches. To verify this, we have followed the reduction process of the nickel precursor in time and explored different nickel growth times of 1, 2, 3, and 5 h. A decrease in the catalytic activity was observed with increasing the reduction time/nickel growth time (Figure 2g). However, the catalytic activity of platinum was preserved with nickel growth time shorter than 5 h, indicating a partial covering of the platinum surface (Figure S5, Supporting Information). After growing nickel for 5 h, platinum catalytic activity was finally hindered, indicating that 5 h is the time point for complete coverage and formation of a thick nickel shell.

After confirming the structure of doxorubicin/platinum–nickel-loaded stomatocytes, we next tested the magnetic response of nickel-containing stomatocytes. A NdFeB magnet (12 mm × 12 mm × 12 mm) was used to generate a magnetic field gradient. With a hand-held gaussmeter, the decay of field strength with increasing distance from the magnetic pole was verified and measured (Figure S6, Supporting Information). The gradient field resulted in movement of the doxorubicin/platinum–nickel-loaded stomatocytes to the vicinity of the magnet, which was clearly visible as demonstrated by the inhomogeneous distribution of the particles in the bulk solution (Figure S7, Supporting Information).

To remotely control the motion, magnetized-nickel-containing stomatocytes (see the Section 3 in the Supporting Information for the magnetization procedure) were exposed to the gradient magnetic field and visualized with confocal microscopy. When the magnet was placed in the left, collective motion of stomatocytes toward areas of higher field strength (left area) was observed (**Figure 3**a, scheme). At a distance of 3.5 cm away (maximum distance used) from the magnet, the magnetic force of magnetized nickel was still sufficient to direct the motion of the stomatocytes. The field strength applied approximately a magnetic torque of 6.0×10^{-19} J on the stomatocytes nanomotors. This was calculated from the formula $\tau = \mu \times B$ (where μ is the magnetic dipole moment $\mu = M \times m_{Ni} = 12$ emu $g^{-1} \times 1.1 \times 10^{-14}$ g; *M*, the saturation magnetization is the reference value,[26] while m_{Ni} or mass of nickel assuming a thickness of nickel layer of 25 nm (from EDX data); B is the field strength 50 Gauss), exceeding the value of rotational thermal energy (2.06×10^{-21} J) by two orders of magnitude. The nickel-containing stomatocytes navigated toward the magnet in the left as indicated by the trajectory path (Figure 3b–d). Three parameters: average velocity, directionality, and displacement of center of mass were used to quantitatively evaluate the directed motion. Directionality, averaged value of Euclidean distance divided by accumulated distance, is a measure of the straightness of motion. The displacement of center of mass describes the average spatial distance between the starting and end points of the stomatocytes, which indicates the migration length. The applied magnetic field could provide a driving force as well as a guiding force to stomatocytes, as illustrated in Figure 3b,c, at both position 0 and position 1, respectively 1.0 ± 0.1 cm and 3.5 ± 0.1 cm away from the magnet. From Figure S6 in the Supporting Information, the exerted field strengths at the two positions were estimated to be 732 ± 28 Gauss and 50 ± 1 Gauss, respectively (corresponding to a gradient of 1576 and 67 Gauss cm^{-1}). By moving toward the magnet, the stomatocyte motors experienced an increase in average velocity from 10.4 (position 1) to 15.0 μm s^{-1} (position 0) as well as a change in directionality from 0.64 to 0.85 (for velocity distribution of stomatocytes motors at both positions, see Figure S8a,b in the Supporting Information). The driving force increases with a decreased distance from the magnet, due to both higher gradient force and torque (Figure 3b,c).

When both a magnetic field and a hydrogen peroxide solution (1.5% v/v) were present (Figure 3d), at position 1 the translation velocity and displacement of center of mass experienced were increased to 13.1 μm s^{-1} and 8.0 μm (compared to 10.4 μm s^{-1} and 5.2 μm for the magnet-only system, Figure 3c). Therefore, the combination of hydrogen peroxide fuel and magnetic attraction led to a directional motion toward the magnetic pole, yet at a higher velocity compared to applying the magnetic field alone. In the presence of the magnet and at position 1, the influence of different hydrogen peroxide concentrations

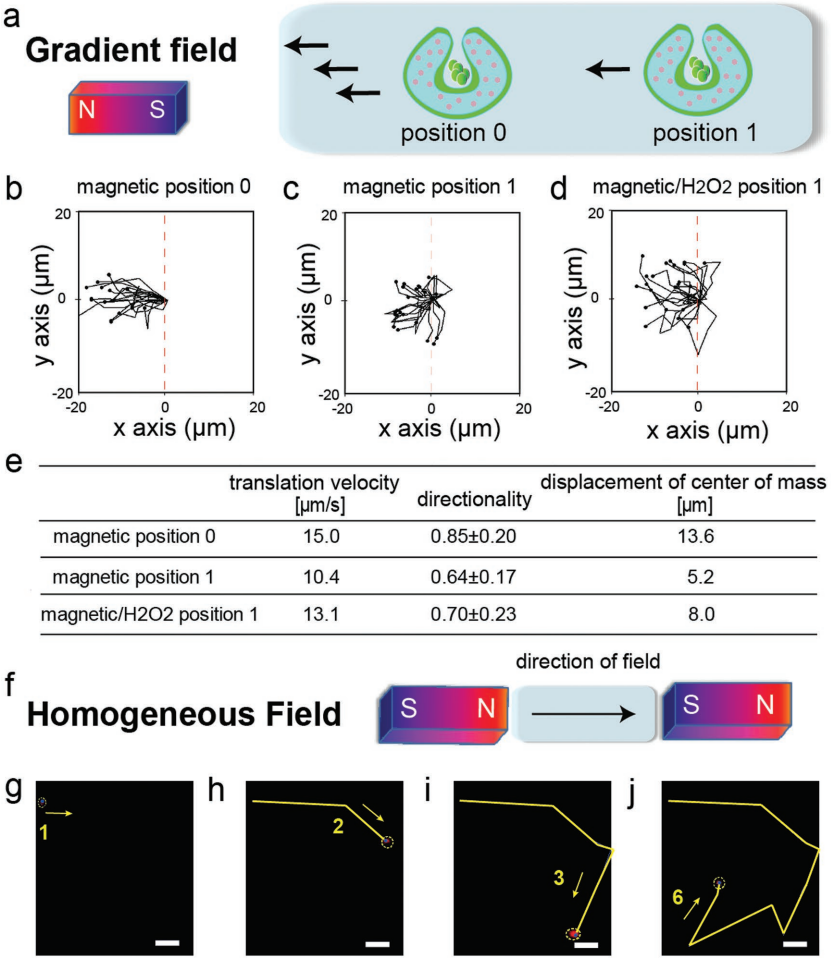

e

	translation velocity [μm/s]	directionality	displacement of center of mass [μm]
magnetic position 0	15.0	0.85±0.20	13.6
magnetic position 1	10.4	0.64±0.17	5.2
magnetic/H2O2 position 1	13.1	0.70±0.23	8.0

Figure 3. a) Schematic illustration of the doxorubicin/platinum–nickel-loaded stomatocytes movement to the left toward higher-gradient magnetic field generated by a NdFeB magnet. b–d) Moving paths over five consecutive frames (time intervals = 268 ms) of the doxorubicin/platinum–nickel-loaded stomatocytes at position 0 (1 ± 0.1 cm away from the magnet) magnet-induced (b); at position 1 (3.5 ± 0.1 cm away from the magnet) magnet-induced (c); at position 1, magnet/hydrogen-peroxide-induced (d). The starting points were normalized to the point of origin. e) Summary table of translation velocity, directionality, and displacement of center of mass for doxorubicin/platinum–nickel-loaded stomatocytes at position 0 with magnet in the left (25 stomatocytes analyzed), at position 1 with magnet in the left (26 stomatocytes analyzed), or at position 1 with both magnet and hydrogen peroxide (24 stomatocytes analyzed). f) Schematic illustration of the experimental set-up for homogeneous magnetic field generated by two parallel magnets. g–j) Confocal fluorescence images of the doxorubicin/platinum–nickel-loaded stomatocyte movement in hydrogen peroxide solution (1.5% v/v) and their sequential steering by changing the direction of the field; time interval between video snapshots = 2304 ms; scale bar is 10 μm.

over the movement was investigated. The stomatocytes motors moved faster with increasing levels of hydrogen peroxide (Figure S8c–e, Supporting Information). Hydrogen peroxide is a biorelevant chemical overproduced by human tumor cell lines[20] (at rates of up to 0.5 nmol/10^4 cells/h, which is significant when related to the size of a tumor). Nevertheless there are also reports regarding its potential harm to healthy cells including DNA lesions, which is concentration-dependent.[27] Here, we used it as a proof of concept to use biorelevant chemicals found in biological systems for propulsion. Attraction toward the magnet was not disturbed at all these hydrogen peroxide levels. In the absence of both fuel and magnetic field, typical Brownian motion was observed (Figure S9a, Supporting Information). The displacement of the center of mass was 2.0 μm. No favored moving direction was observed. The directionality was 0.45, significantly lower than in the presence of magnetic field/hydrogen peroxide. The average mean square displacement versus time interval curve (Supporting Information Figure S9b) showed a linear dependence, which fits the Brownian motion, demonstrating that the stomatocytes move under random walking when without fuel and magnetic field.

In addition to velocity as discussed above, moving direction can be governed by the profile of the applied field. Nickel-containing stomatocytes could readily sense the position change of the magnet and reorient their motion accordingly (Figure S11, Supporting Information). The reorientation could be achieved repeatedly.

Besides the gradient field, we can also apply a homogeneous magnetic field by sandwiching the magnetized doxorubicin/platinum–nickel-loaded stomatocytes solution between two parallel magnets (NdFeB magnet, 12 mm × 12 mm × 12 mm) (Figure 3f). By changing only the direction of the magnetic field (Figure 3g–j, and Figure S12a–g, Supporting Information) not the positions of the magnets, we could precisely control the moving direction of the motors. After removing the external homogeneous field, dispersive movement with no favored direction was observed (Supporting Information Figure S12h–l).

To test the transportation abilities of the stomatocyte motors in tissue, a tissue model was established by using microfluidic technology (illustrated in **Figure 4**). The microslide consists of two chambers, which are connected through a narrow channel in the middle. In mimicking tissue,[28] first collagen (1 mg mL^{-1}) was used to form a gel network (mesh size ≈ 10 μm, in agreement with previous report[29]) (Figure 4a,c, scanning electron microscopy image and bright-field image) in the left chamber and middle channel. After the gel formation, diluted motor solution was added to the right channel. A low concentration of motors was used to avoid instant formation of bundles and hindered entrance into gel (2.8×10^9 particles per mL). The motors demonstrated Brownian motion (Figure S13, Supporting Information). Then, a magnet (NdFeB, 12 mm × 12 mm × 12 mm) was placed on the left. Figure 4f–k show the gel boundary area. Stomatocyte motors could sense the magnetic field and be readily guided toward the gel mesh on the left. Upon entering the gel matrix (the blue

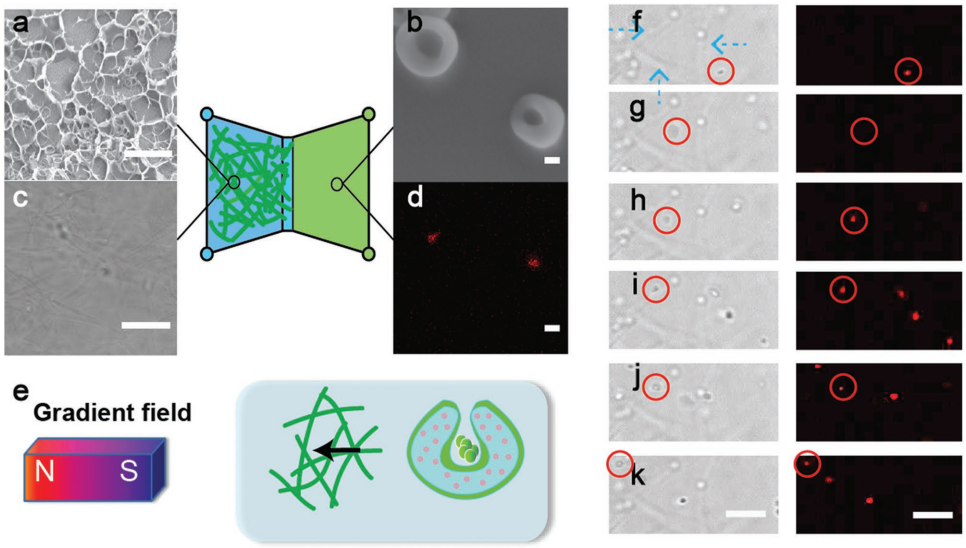

Figure 4. a) Cryo-scanning electron microscopy (cryo-SEM) image of gel matrix, scale bar = 10 µm. b) Scanning electron microscopy (SEM) image of doxorubicin/platinum–nickel-loaded stomatocytes, scale bar = 100 nm. c) Confocal bright field image of gel matrix, scale bar = 10 µm. d) Fluorescent image of doxorubicin and platinum–nickel-loaded stomatocytes, scale bar represents 1 µm. e) Scheme of the magnetic guidance of doxorubicin/platinum–nickel-loaded stomatocytes toward gel matrix. f–k) Doxorubicin/platinum–nickel-loaded stomatocytes could be guided through a collagen gel matrix by applying an external magnetic field (particle in red circle), video snapshots, time intervals 1.34 s, scale bar = 10 µm.

arrows in Figure 4 point to the fibrils in a triangular gel mesh), the nanomotors demonstrated a guided motion through the gel mesh (Figure 4 and Figure S14 in the Supporting Information). The velocity of motors was 12.4 µm s^{-1}. The tracking path of motors was shown in Figure S15 in the Supporting Information. Tuning the collagen concentration can vary the gel mesh density/crosslinking density of the collagen gel. By increasing the concentration to 1.5 mg mL^{-1} from 1 mg mL^{-1}, we obtained a gel with a decreased mesh size of 6 µm, which is in agreement with the literature data.[29] At this gel pore size, the movement of the stomatocytes remained unhindered, in their guided motion toward the magnetic pole (Figure S16, Supporting Information). After demonstrating the possibility of achieving guided motion in the pure gel, we replaced the gel with a gel laden with human cervical cancer HeLa cells as a mimic of a tumor tissue. **Figure 5**a shows schematically

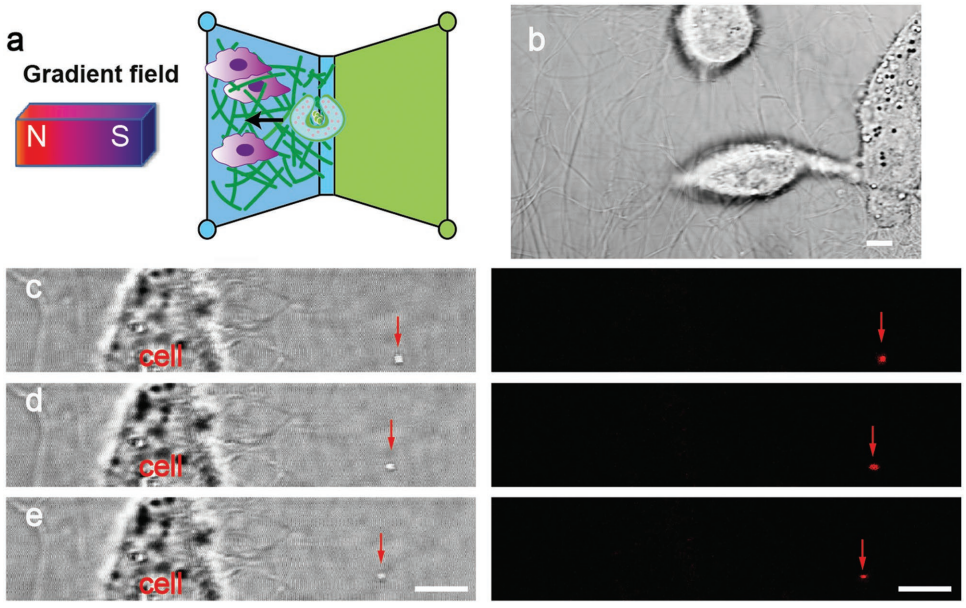

Figure 5. a) Schematic representation of the magnetic guidance of doxorubicin/platinum–nickel-loaded stomatocytes through HeLa-cell-laden gel matrix. b) Confocal bright-field image of HeLa-cell-laden gel; the scale bar represents 10 µm; c–e) Doxorubicin/platinum–nickel-loaded stomatocytes could be guided toward a cell in the collagen gel mesh by applying an external magnetic field (particle indicated by the red arrow), left: bright field; right: fluorescent field; tracking trajectories over three frames; time intervals 268 ms; scale bar = 10 µm.

the experimental design of magnetic-guided motion of nickel-containing stomatocytes toward cell-laden gel. After placing the magnet to the left, stomatocytes loaded with doxorubicin and platinum–nickel moved forward toward the magnet and traveled through the HeLa-cell-laden gel matrix (Figure 5c–e). Collective motion toward the left where the magnetic field strength was stronger is demonstrated in Figure S17 in the Supporting Information.

In summary, we fabricated magnetic nanomotors by using a convenient and mild bottom-up approach and have presented a method to achieve directional control over nanometer-scale stomatocyte motors. Stomacytes with incorporated nickel–platinum particles allowed both hydrogen peroxide/magnetic locomotion and remote magnetic guidance. Finally, we have also shown that the nanomotors can be guided through a tissue model formed from a collagen gel. Capable of steerable motion at a relatively high speed, the motors could transport drug molecules in a targeted specific way and hold promise for precise localized tissue drug delivery.

Supporting Information

Supporting Information is available from the Wiley Online Library or from the author.

Acknowledgements

F.P. and Y.T. contributed equally to this work. This work was supported by the European Research Council under the European Union's Seventh Framework Programme (Grant No. FP7/2007-20012)/ERC-StG 307679 "StomaMotors". The authors acknowledge support from the Ministry of Education, Culture and Science (Gravitation program 024.001.035). F. Peng acknowledges funding from China scholarship council. Geert-Jan Janssen and the General Instruments department are acknowledged for providing support for the Cryo-SEM, SAED, ICP-MS, and EDX measurements.

Received: September 16, 2016
Revised: October 6, 2016
Published online: November 28, 2016

[1] R. F. Ismagilov, A. Schwartz, N. Bowden, G. M. Whitesides, *Angew. Chem., Int. Ed.* **2002**, *41*, 652.
[2] a) M. Schliwa, G. Woehlke, *Nature* **2003**, *422*, 759; b) R. L. Cross, *Nature* **2004**, *427*, 407.
[3] A. Bahat, I. Tur-Kaspa, A. Gakamsky, L. C. Giojalas, H. Breitbart, M. Eisenbach, *Nat. Med.* **2003**, *9*, 149.
[4] a) A. A. Solovev, W. Xi, D. H. Gracias, S. M. Harazim, C. Deneke, S. Sanchez, O. G. Schmidt, *ACS Nano* **2012**, *6*, 1751; b) D. Kagan, M. J. Benchimol, J. C. Claussen, E. Chuluun-Erdene, S. Esener, J. Wang, *Angew. Chem., Int. Ed.* **2012**, *51*, 7519.
[5] a) D. Kagan, R. Laocharoensuk, M. Zimmerman, C. Clawson, S. Balasubramanian, D. Kang, D. Bishop, S. Sattayasamitsathit, L. Zhang, J. Wang, *Small* **2010**, *6*, 2741; b) W. Gao, J. Wang, *Nanoscale* **2014**, *6*, 10486; c) F. Peng, Y. Tu, J. C. van Hest, D. A. Wilson, *Angew. Chem., Int. Ed.* **2015**, *54*, 11662; d) S. Tottori, L. Zhang, F. Qiu, K. K. Krawczyk, A. Franco-Obregon, B. J. Nelson, *Adv. Mater.* **2012**, *24*, 811; e) K. Kim, X. B. Xu, J. H. Guo, D. L. Fan, *Nat. Commun.* **2014**, *5*, 3632; f) X. Xu, K. Kim, D. Fan, *Angew. Chem., Int. Ed.* **2015**, *54*, 2525.
[6] a) L. K. E. A. Abdelmohsen, F. Peng, Y. F. Tu, D. A. Wilson, *J. Mater. Chem. B* **2014**, *2*, 2395; b) B. Jurado-Sanchez, A. Escarpa, J. Wang, *Chem. Commun.* **2015**, *51*, 14088; c) B. Esteban-Fernandez de Avila, A. Martin, F. Soto, M. A. Lopez-Ramirez, S. Campuzano, G. M. Vasquez-Machado, W. Gao, L. Zhang, J. Wang, *ACS Nano* **2015**, *9*, 6756.
[7] E. S. Olson, J. Orozco, Z. Wu, C. D. Malone, B. Yi, W. Gao, M. Eghtedari, J. Wang, R. F. Mattrey, *Biomaterials* **2013**, *34*, 8918.
[8] a) L. Soler, S. Sanchez, *Nanoscale* **2014**, *6*, 7175; b) W. Gao, X. M. Feng, A. Pei, Y. E. Gu, J. X. Li, J. Wang, *Nanoscale* **2013**, *5*, 4696.
[9] a) J. R. Howse, R. A. L. Jones, A. J. Ryan, T. Gough, R. Vafabakhsh, R. Golestanian, *Phys. Rev. Lett.* **2007**, *99*, 048102; b) T. C. Lee, M. Alarcon-Correa, C. Miksch, K. Hahn, J. G. Gibbs, P. Fischer, *Nano Lett.* **2014**, *14*, 2407; c) P. H. Colberg, S. Y. Reigh, B. Robertson, R. Kapral, *Acc. Chem. Res.* **2014**, *47*, 3504.
[10] S. Sanchez, A. N. Ananth, V. M. Fomin, M. Viehrig, O. G. Schmidt, *J. Am. Chem. Soc.* **2011**, *133*, 14860.
[11] a) T. R. Kline, W. F. Paxton, T. E. Mallouk, A. Sen, *Angew. Chem., Int. Ed.* **2005**, *44*, 744; b) V. Magdanz, S. Sanchez, O. G. Schmidt, *Adv. Mater.* **2013**, *25*, 6581; c) S. Sanchez, L. Soler, J. Katuri, *Angew. Chem., Int. Ed.* **2015**, *54*, 1414.
[12] A. A. Solovev, E. J. Smith, C. C. B. Bufon, S. Sanchez, O. G. Schmidt, *Angew. Chem., Int. Ed.* **2011**, *50*, 10875.
[13] a) S. Sengupta, K. K. Dey, H. S. Muddana, T. Tabouillot, M. E. Ibele, P. J. Butler, A. Sen, *J. Am. Chem. Soc.* **2013**, *135*, 1406; b) B. ten Hagen, F. Kummel, R. Wittkowski, D. Takagi, H. Lowen, C. Bechinger, *Nat. Commun.* **2014**, *5*, 4829; c) G. J. Zhao, M. Pumera, *Langmuir* **2013**, *29*, 7411; d) L. Baraban, S. M. Harazim, S. Sanchez, O. G. Schmidt, *Angew. Chem., Int. Ed.* **2013**, *52*, 5552.
[14] a) F. Popp, J. P. Armitage, D. Schuler, *Nat. Commun.* **2014**, *5*, 5398; b) A. P. Chen, V. M. Berounsky, M. K. Chan, M. G. Blackford, C. Cady, B. M. Moskowitz, P. Kraal, E. A. Lima, R. E. Kopp, G. R. Lumpkin, B. P. Weiss, P. Hesse, N. G. F. Vella, *Nat. Commun.* **2014**, *5*, 4797; c) S. Martel, M. Mohammadi, O. Felfoul, Z. Lu, P. Pouponneau, *Int. J. Robot. Res.* **2009**, *28*, 571.
[15] a) Z. Luo, K. Y. Cai, Y. Hu, J. H. Li, X. W. Ding, B. L. Zhang, D. W. Xu, W. H. Yang, P. Liu, *Adv. Mater.* **2012**, *24*, 431; b) P. Saint-Cricq, S. Deshayes, J. I. Zink, A. M. Kasko, *Nanoscale* **2015**, *7*, 13168.
[16] J. M. Shin, R. M. Anisur, M. K. Ko, G. H. Im, J. H. Lee, I. S. Lee, *Angew. Chem., Int. Ed.* **2009**, *48*, 321.
[17] a) A. Celedon, I. M. Nodelman, B. Wildt, R. Dewan, P. Searson, D. Wirtz, G. D. Bowman, S. X. Sun, *Nano Lett.* **2009**, *9*, 1720; b) R. M. Erb, N. J. Jenness, R. L. Clark, B. B. Yellen, *Adv. Mater.* **2009**, *21*, 4825; c) R. S. M. Rikken, R. J. M. Nolte, J. C. Maan, J. C. M. van Hest, D. A. Wilson, P. C. M. Christianen, *Soft Matter* **2014**, *10*, 1295; d) A. La Porta, M. D. Wang, *Phys. Rev. Lett.* **2004**, *92*, 190801; e) S. Gangwal, O. J. Cayre, M. Z. Bazant, O. D. Velev, *Phys. Rev. Lett.* **2008**, *100*, 058302.
[18] a) L. Baraban, D. Makarov, R. Streubel, I. Monch, D. Grimm, S. Sanchez, O. G. Schmidt, *ACS Nano* **2012**, *6*, 3383; b) D. Schamel, A. G. Mark, J. G. Gibbs, C. Miksch, K. I. Morozov, A. M. Leshansky, P. Fischer, *ACS Nano* **2014**, *8*, 8794.
[19] P. Mandal, V. Chopra, A. Ghosh, *ACS Nano* **2015**, *9*, 4717.
[20] T. P. Szatrowski, C. F. Nathan, *Cancer Res.* **1991**, *51*, 794.
[21] a) Z. Wu, Y. Wu, W. He, X. Lin, J. Sun, Q. He, *Angew. Chem., Int. Ed.* **2013**, *52*, 7000; b) Y. Wu, Z. Wu, X. Lin, Q. He, J. Li, *ACS Nano* **2012**, *6*, 10910; c) X. Lin, Z. Wu, Y. Wu, M. Xuan, Q. He, *Adv. Mater.* **2016**, *28*, 1060; d) Z. Wu, T. Si, W. Gao, X. Lin, J. Wang, Q. He, *Small* **2016**, *12*, 577.

[22] a) D. A. Wilson, R. J. M. Nolte, J. C. M. van Hest, *Nat. Chem.* **2012**, *4*, 268; b) D. A. Wilson, R. J. M. Nolte, J. C. M. van Hest, *J. Am. Chem. Soc.* **2012**, *134*, 9894.
[23] a) M. Sanles-Sobrido, M. Perez-Lorenzo, B. Rodriguez-Gonzalez, V. Salgueirino, M. A. Correa-Duarte, *Angew. Chem., Int. Ed.* **2012**, *51*, 3877; b) M. Grzelczak, M. A. Correa-Duarte, V. Salgueirino-Maceira, B. Rodriguez-Gonzalez, J. Rivas, L. M. Liz-Marzan, *Angew. Chem., Int. Ed.* **2007**, *46*, 7026.
[24] D. A. Wilson, B. de Nijs, A. van Blaaderen, R. J. M. Nolte, J. C. M. van Hest, *Nanoscale* **2013**, *5*, 1315.
[25] a) X. L. Sun, S. J. Guo, C. S. Chung, W. L. Zhu, S. H. Sun, *Adv. Mater.* **2013**, *25*, 132; b) G. W. Wu, S. B. He, H. P. Peng, H. H. Deng, A. L. Liu, X. H. Lin, X. H. Xia, W. Chen, *Anal. Chem.* **2014**, *86*, 10955.
[26] M. Sanles-Sobrido, M. Banobre-Lopez, V. Salgueirino, M. A. Correa-Duarte, B. Rodriguez-Gonzalez, J. Rivas, L. M. Liz-Marzan, *J. Mater. Chem.* **2010**, *20*, 7360.
[27] J. Nakamura, E. R. Purvis, J. A. Swenberg, *Nucleic Acids Res.* **2003**, *31*, 1790.
[28] a) M. D. Tang, A. P. Golden, J. Tien, *Adv. Mater.* **2004**, *16*, 1345; b) N. Sasaki, C. Bos, J. M. Escoffre, G. Storm, C. Moonen, *Int. J. Pharm.* **2015**, *482*, 118.
[29] P. Banerjee, D. Lenz, J. P. Robinson, J. L. Rickus, A. K. Bhunia, *Lab Invest.* **2008**, *88*, 196.